

Signal identification with Kalman Filter towards background-free neutrinoless double beta decay searches in gaseous detectors

Tao Li,² Shaobo Wang,^{1,3,*} Yu Chen,² Ke Han,^{1,†} Heng Lin,¹ Kaixiang Ni,¹ Wei Wang,² Yiliu Xu,³ and An'ni Zou³

¹*INPAC; Shanghai Laboratory for Particle Physics and Cosmology;*

Key Laboratory for Particle Astrophysics and Cosmology (MOE),

School of Physics and Astronomy, Shanghai Jiao Tong University, Shanghai 200240, China

²*School of Physics, Sun Yat-Sen University, Guangzhou, 510215, China*

³*SPEIT (SJTU-ParisTech Elite Institute of Technology),*

Shanghai Jiao Tong University, Shanghai, 200240, China

(Dated: December 23, 2024)

Particle tracks and differential energy loss measured in high pressure gaseous detectors can be exploited for event identification in neutrinoless double beta decay ($0\nu\beta\beta$) searches. We develop a new method based on Kalman Filter in a Bayesian formalism (KFB) to reconstruct meandering tracks of MeV-scale electrons. With simulation data, we compare the signal and background discrimination power of the KFB method assuming different detector granularities and energy resolutions. Typical background from ^{232}Th and ^{238}U decay chains can be suppressed by another order of magnitude than that in published literatures, approaching the background-free regime. For the proposed PandaX-III experiment, the $0\nu\beta\beta$ search half-life sensitivity at the 90% confidence level would reach 2.7×10^{26} yr with 5-year live time, a factor of 2.7 improvement over the initial design target.

Neutrinoless double beta decay ($0\nu\beta\beta$) is a hypothetical weak decay process that would confirm the Majorana nature of neutrinos and provide a direct evidence of lepton number violation [1, 2]. Experimental search for $0\nu\beta\beta$ has been an active frontier in particle and nuclear physics [3]. The Standard-Model-allowed two neutrino double beta decay ($2\nu\beta\beta$) has been observed in more than ten isotopes. Searches for the $0\nu\beta\beta$ utilize those isotopes, including ^{136}Xe , ^{76}Ge , and ^{130}Te . The current lower half-life limits for $0\nu\beta\beta$ of the three isotopes are 1.07×10^{26} yr, 1.8×10^{26} yr, and 3.2×10^{25} yr (90% confidence level, or CL), established by KamLAND-Zen, GERDA, and CUORE experiments respectively [4–6]. Most $0\nu\beta\beta$ experiments identify possible signals by event excess around the decay Q-value in the summed electron energy spectrum.

Xenon-based high pressure gaseous Time Projection Chambers (TPCs) can utilize topological features of event tracks and differential energy loss to identify possible ^{136}Xe $0\nu\beta\beta$ signals. Two emitted electrons carry the Q-value of 2458 keV and may travel \mathcal{O} (10 cm) along meandering tracks in 10 bar xenon gas. Signal identification with tracks in a ^{136}Xe gaseous TPC has been exploited early on by the Gotthard experiment [7]. More recently, the NEXT experiment [8] demonstrated the effective track reconstruction with electroluminescence amplification signals in their prototype TPC [9]. Efficiencies of signal and background identification in the proposed PandaX-III gaseous TPC [10] have been studied with simulation data [11, 12]. The aforementioned experiments utilize the prominent Bragg Blob (BB) feature of event tracks. Each end of a $0\nu\beta\beta$ track has a BB, in which rapid energy loss in unit volume happens because of increased differential energy loss (Bragg peak) and larger

scattering angles right before an electron stops.

Our study aims to extract additional topological features by reconstructing the meandering tracks with Kalman Filter in a Bayesian formalism (KFB) [13, 14]. Differential energy loss along tracks and particle momentum by the end of the tracks can be calculated and used for the signal and background identification. When combined with parameters such as track energies, we demonstrate that almost all the background in the region of interest (ROI) of $0\nu\beta\beta$ search can be rejected and the search sensitivity further improved in a typical low-background gaseous TPC.

To demonstrate the performance of the KFB approach, we construct a conceptual high pressure gaseous TPC with the Geant4 simulation framework [15]. The geometry is similar to the PandaX-III TPC [16]. The active volume (AV) is 1.6 m in diameter and 1.2 m high, which contains approximately 140 kg of xenon gas (with 90% ^{136}Xe) at 10 bar. The cathode and the readout plane are placed at the two bases of the cylindrical AV respectively. Outside of the AV, we construct an acrylic field cage, copper shielding liner, stainless steel vessel, lead shielding, and high-density polyethylene shielding in sequence. The dimensions of each component are identical to Ref. [17]. The $0\nu\beta\beta$ signals are produced with the Decay0 package [18], which gives the angular and energy distributions of two emitted electrons. Background events from the decay chains of ^{232}Th and ^{238}U in the detector components and shielding layers are considered.

The detector response of TPC, including electron diffusion, readout schemes, and energy resolution, is simulated in the REST framework [12]. While drifting to the readout plane, ionization electrons diffuse transversely and longitudinally which results in broadening of the

tracks. The transverse (longitudinal) diffusion coefficient is set to be $1.0(1.5) \times 10^{-2} \text{ cm}^{1/2}$, assuming xenon is mixed with a quencher gas such as Trimethylamine to have reduced diffusions.

We have performed our studies under five different configurations by varying the readout schemes and detector energy resolutions. In the first two high granularity configurations, the detector's readout plane is fully instrumented with $1 \text{ mm} \times 1 \text{ mm}$ pixels. An energy resolution of 3% (Full Width at Half Maximum, FWHM) at the Q-value is assumed for the first one and 6% for the second. We compare such detectors with configurations of degraded spatial granularity of $3 \text{ mm} \times 3 \text{ mm}$ and energy resolution of 3% and 1% respectively. The last configuration replicates the PandaX-III detector specifications. The readout plane is covered with 52 pieces of $20 \text{ cm} \times 20 \text{ cm}$ readout modules, each of which is equipped with 3-mm-wide readout strips. Each strip reads out signals from 64 connected pixels in horizontal or vertical directions. The setup significantly reduces the number of readout channels needed, but does introduce ambiguity in track reconstruction. It is also worth noting that efficiency loss is considered because the TPC's AV is not 100% monitored by readout modules in this configuration. The energy resolution is 3% in this configuration. Later we will refer the configurations as $(1 \text{ mm}, 3\%)$, $(1 \text{ mm}, 6\%)$, $(3 \text{ mm}, 3\%)$, $(3 \text{ mm}, 1\%)$, and $(3 \text{ mm strip}, 3\%)$ respectively. Once reaching the readout plane, ionization electrons register *charge signal hits* (or *hits* for short) in pixels or strips. The amplitude and timing of hits contain all the information that can be collected in a physical detector. The output hit data from our simulation would mimic detector data.

The simulation data are preprocessed in two phases before reconstruction with the KFB approach. Firstly, we group hits of an event into a principal track and subordinate track(s) based on the distance among the hits. The grouping is implemented with a widely-used clustering algorithm called DBSCAN [19]. An example of well-separated principal and subordinate tracks of a background event is shown in Fig. 1. Once the tracks defined, the total deposited energy of the principal track E_p can be calculated. Both the $0\nu\beta\beta$ signals and the backgrounds may have the multiple tracks, but background events from γ -rays are more fragmented and hence have smaller E_p in general. Secondly, the principal track is reconstructed roughly. Hits of the principal track are divided into segments with the Birch clustering algorithm [20], shown as groups of colored dots in Fig. 1. The charge-weighted centers of segments, named Birch clusters (BCs), are shown as green dots. They are sorted by an Ant Colony Optimization algorithm [21] with random starting points. The algorithm enumerates different connections of BCs and finds the one with the shortest total track length. The number of segments is optimized to balance sorting quality and computing loads.

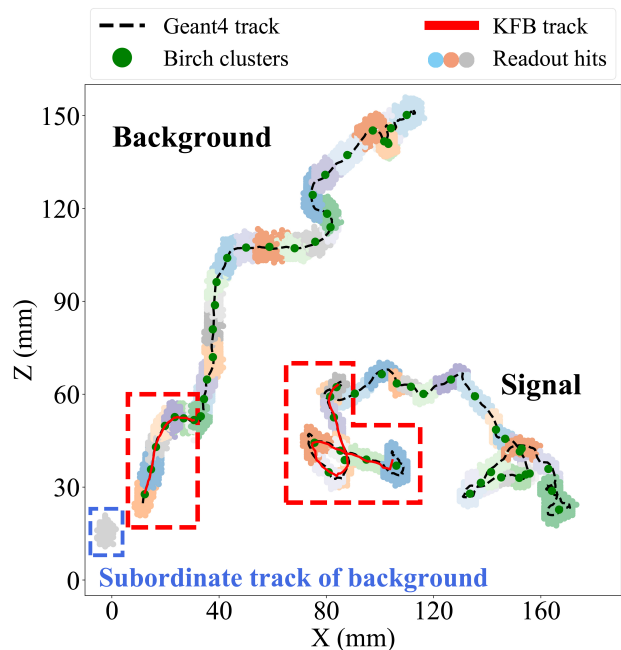


FIG. 1. Example background (left) and $0\nu\beta\beta$ signal (right) events generated in simulation. The tracks are projected in the XZ plane, where X is one of the transverse directions and Z is the longitudinal direction along the drift field. The signal event is enlarged by 1.5 times for easier comparison.

The Kalman Filter is then introduced to refine the reconstruction of the tracks [22, 23]. We define a state vector $s = (x, y, z, u_x, u_y, u_z)^T$, including the three dimensional position and unit velocity vector along the track. The physical process of multiple scattering between two adjacent steps $k-1$ and k can be written as: $s_k = F s_{k-1} + \omega_k$, where F is the propagation matrix of uniform rectilinear motion and ω_k is the process noise. ω_k can be described as $\omega_k = (0, 0, 0, G(0, \theta_x), G(0, \theta_y), G(0, \theta_z))^T$, where G is the standard Gaussian distribution and $\theta_{x,y,z}$ represents the projection of scattering angle θ_{space}^{rms} in three directions. For an electron with momentum p , Coulomb scattering distribution follows Gaussian approximation for the Molière's formula [24]:

$$\theta_{space}^{rms} = \frac{19.2 \text{ MeV}}{pv} \sqrt{\lambda} [1 + 0.038 \ln \lambda], \quad (1)$$

where v is the particle velocity, and λ is the step size in the unit of radiation length in the medium. Energy deposition is not considered to simplify our physics model. Measurement data are anchored by the BCs. In between adjacent BCs, the steps $m_k = (x^m, y^m, z^m)^T$ are linearly interpolated hit points spaced by the detector granularity. The associated measurement noise is $\delta_k = (G(0, \sigma), G(0, \sigma), G(0, \sigma))^T$, where measurement uncertainty σ includes contributions from detector spatial resolution and uncertainties introduced in the pre-

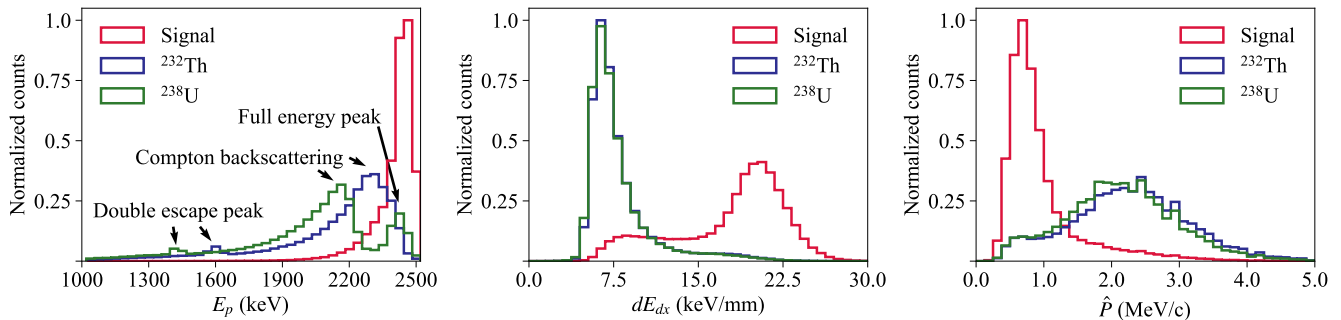


FIG. 2. Distributions of three parameters from the KFB workflow. The Y axis is normalized by the highest value in each plot.

processing.

With Bayesian formalism, Kalman Filter can determine the values of process noise ω_k and measurement noise δ_k [13, 14], the covariance matrices of which are denoted as Q and R , respectively. With all the measurements up to the step k , $\mathcal{M}_k = \{m_1, m_2, \dots, m_k\}$, we can evaluate the probability of having (Q_k, R_k) ,

$$P(Q_k, R_k | \mathcal{M}_k) \propto P(m_k | \mathcal{M}_{k-1}, Q_k, R_k) \times P(Q_{k-1}, R_{k-1} | \mathcal{M}_{k-1}), \quad (2)$$

The values θ_{space}^{rms} and σ at the step k are determined by maximizing the above probability. Subsequently, we update the state vector and covariance matrices and are ready for filtering at the step $k + 1$.

The differences between signal and background tracks are expected to be the largest at the two ends. We filter 20% of the track by two ends with KFB respectively. In Fig. 1, the dashed red rectangle (L-shaped polygon) marks one end of the background (signal) track used for filtering. The dashed black track represents the true trajectory of events in Geant4 simulation. One can see the KFB tracks match the MC-truth reasonably well.

We extract two additional parameters from the KFB tracks. Energy loss per unit travel length dE/dx can be calculated more precisely along the reconstructed track. We refer the smaller of two dE/dx values at two ends of a track as dE_{dx} . Compared to BB, dE_{dx} is more representative of the Bragg peak of energy loss. With θ_{space}^{rms} determined in KFB, momenta at the ends of the reconstructed track can also be estimated from Eq. 1. We define \hat{P} as the larger of momenta at two ends.

Besides E_p , dE_{dx} , and \hat{P} , other common parameters could also be calculated more accurately with the KFB approach. The parameter E_{Space} defines energy in a unit volume around the energy-weighted center of the event and represents the fragmentation of tracks. For pixel (strip) readout, the unit volume is a sphere (circle) with a radius of 60 mm, the size of which is optimized for signal and background discrimination. In addition, the number of tracks N_{Tracks} , and energy of BB E_{BB} are calculated

and used to further improve event identification.

The distributions of E_p , dE_{dx} and \hat{P} for the (1 mm, 3%) configuration are shown in Fig. 2. In the E_p distribution of background, double escape peaks, Compton backscattering peaks, and a full absorption peak at 2447 keV are visible and marked. The majority of $0\nu\beta\beta$ signals deposit most of the energy in principal tracks and the E_p distribution is concentrated within the ROI. The most effective parameter for the signal and background discrimination is dE_{dx} . The dE_{dx} of signals is mostly in the range 15 to 30 keV/mm, but background less than 10 keV/mm. Signal events with dE_{dx} less than 15 keV/mm are mainly the ones that two electrons share extremely lopsided partition of the Q-value and resemble a background event physically. The distribution of \hat{P} for signal is mainly concentrated in less than 1 MeV/c region, while background is above 1.5 MeV/c. An excess of background events around 1 MeV/c is due to misidentification of the principal track. When subordinate tracks are too close to the principal one, DBSCAN may group them together and result in smaller \hat{P} values from KFB.

E_p , dE_{dx} , and \hat{P} are used as rectangular cuts and the results are shown in Table I for the five configurations. We define the discrimination significance $\Xi = \epsilon_s / \sqrt{\epsilon_b}$, where ϵ_s is the signal efficiency and ϵ_b the background efficiency after the cuts. In the (1 mm, 3%) configuration, the background rate of ^{232}Th is suppressed by more than three orders of magnitude while keeping ϵ_s at about 30%, and the corresponding Ξ is 12.7. The discrimination for ^{238}U chain is less significant because the 2447 keV full absorption peak of ^{214}Bi overlaps with signals in E_p . In the 1 mm-low-resolution case, Ξ decreases evidently because the Compton backscattering peak of ^{208}Tl contaminates the wider ROI, similar to what 2447 keV peak does for all configurations. Compare to the low granularity case with the same energy resolution, Ξ decreases only slightly in the (3 mm, 3%) configuration because the 1-mm granularity is an over-kill for diffused tracks in a TPC. Under the (3 mm, 1%) condition, Ξ is up to 13.8 (8.3) for ^{232}Th (^{238}U), thanks to better determination of

TABLE I. Effects of rectangular cuts and BDT cuts on ϵ_s , ϵ_b , and Ξ in the five configurations. Background events from ^{232}Th and ^{238}U are considered separately.

Configurations	Rectangular Cuts						BDT Cuts					
	^{232}Th			^{238}U			^{232}Th			^{238}U		
	ϵ_s	ϵ_b	Ξ	ϵ_s	ϵ_b	Ξ	ϵ_s	ϵ_b	Ξ	ϵ_s	ϵ_b	Ξ
(1 mm, 3%)	0.30	5.6×10^{-4}	12.7	0.53	4.6×10^{-3}	7.8	0.34	4.7×10^{-4}	15.7	0.49	2.8×10^{-3}	9.3
(1 mm, 6%)	0.34	2.3×10^{-3}	7.1	0.47	3.7×10^{-3}	7.7	0.35	1.2×10^{-3}	10.1	0.57	4.2×10^{-3}	8.8
(3 mm, 3%)	0.25	3.9×10^{-4}	12.7	0.49	4.7×10^{-3}	7.1	0.39	6.7×10^{-4}	15.1	0.51	3.4×10^{-3}	8.7
(3 mm, 1%)	0.36	6.8×10^{-3}	13.8	0.26	9.9×10^{-4}	8.3	0.50	8.2×10^{-4}	17.5	0.40	1.5×10^{-3}	10.3
(3 mm strip, 3%)	0.23	1.0×10^{-3}	7.3	0.30	4.3×10^{-3}	4.6	0.32	8.3×10^{-4}	11.1	0.46	4.6×10^{-3}	6.8

E_p . For the strip-readout scheme, the discrimination significance Ξ of ^{232}Th and ^{238}U is reduced to 7.3 and 4.6 respectively.

The three parameters are used in a BDT (Boosted Decision Trees) based on the Toolkit for MultiVariate Analysis [25]. BDT classifies signal and background with complicated contours in a multi-dimensional parameter space established by training data. Compared with the rectangular cuts, the improvement of Ξ is smaller than 5% for all configurations with pixel readout, which demonstrates the orthogonality of the three parameters. For the strip readout configuration, the tracks are reconstructed in two two-dimensional planes independently and two sets of dE_{dx} and \hat{P} are obtained. The BDT cuts get more effective and increase Ξ by approximately 20%.

When E_{Space} , N_{Track} , and E_{BB} are added as input for BDT as well, we observe additional 20% improvement in discrimination power approximately for all configurations. The best Ξ we achieve is 17.4 (10.3) for ^{232}Th (^{238}U) in the (3 mm, 1%) configuration. Table I shows the results of BDT cuts with all the input parameters.

To illustrate the effectiveness of event discrimination, we calculate the background levels and $0\nu\beta\beta$ search sensitivity of the PandaX-III experiment with topological cuts. Background contributions from all components mentioned in the MC geometry are considered. Assumed radioactivity levels of the detector materials are the same as in Ref. [10]. Without any topological cuts, the background level is 152 counts per year (CPY) in the ROI, which is defined as $0.85 \times \text{FWHM}$ (i.e., twice the standard deviation of a Gaussian peak) around the Q-value. The ^{232}Th chain contributes to 74% of the background events and the ^{238}U chain 26%. The majority of the background is from the acrylic field cage, the copper liner, and the stainless vessel.

The BDT is re-trained with mixed ^{232}Th and ^{238}U backgrounds and cut criteria re-adjusted to maximize the search sensitivity of $0\nu\beta\beta$. Fig. 3 shows the signal and background spectra before and after BDT cuts. Within ROI, the optimized BDT cuts suppress background by

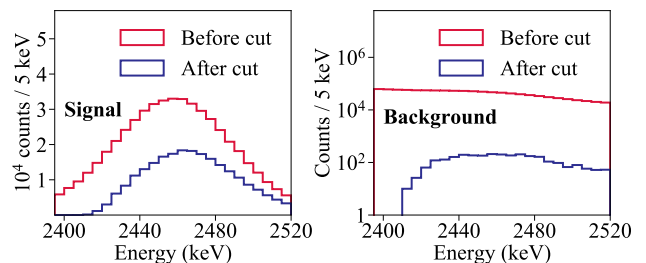


FIG. 3. Effects of BDT cuts for the signal (left) and background (right). Events with energy less than 2410 keV are rejected because of the E_p cut.

3.2×10^{-3} , resulting a background of 0.49 CPY. The corresponding signal efficiency of topological cuts is 50% and the overall efficiency is 35%. Compared with the design target [10], the background rate is 10.4 times lower, thanks to the BDT cuts based on KFB tracks. The background rate is 3.1 times smaller than the one with the topological cuts developed in Ref. [12] and meanwhile the signal efficiency is 1.5 times higher. Assuming null results, the exclusion limits are established following a method outlined in Ref. [26] to take into account of Poissonian fluctuation of small background values. The exclusion sensitivity of PandaX-III is 2.7×10^{26} yr (90% CL) with 5-year live time, a factor of 2.7 or 2.4 improvement comparing to the two cases.

In summary, we present a Kalman Filter based reconstruction workflow for meandering tracks of MeV-scale electrons traveling in a high pressure gas medium. With Monte Carlo simulated data, we apply the technique to $0\nu\beta\beta$ searches, and demonstrate a significant improvement in signal and background discrimination. Five different configurations of readout schemes and energy resolutions for a gaseous TPC are compared in terms of discrimination power. Impact of the spatial granularity of 1 mm and 3 mm is marginal, partially because track width due to electron diffusion is nominally larger than detector granularity. On the other hand, deterioration

of energy resolution can negatively affect the identification of background events from ^{232}Th and lower the discrimination power. For the best configuration of 3 mm granularity and 1% resolution, cuts based on the BDT classifier can suppress ^{232}Th (^{238}U) background by a factor of 8.3×10^{-4} (1.5×10^{-3}), while keeping 50% (40%) of the signals. In our simulated detector, a background rate of 0.11 CPY is achieved with a signal efficiency of 40%. Equivalently less than one background event is expected in 5 years, pushing the search towards background-free regime.

With a strip-readout scheme as the one currently used in PandaX-III, we can still suppress the background by a factor of more than 300 while keeping at least 50% of the signal with topological cuts from our improved track reconstruction. After the traditional calorimeter cuts and BDT cuts, the background rate is 0.49 CPY for PandaX-III, and the corresponding half-life sensitivity to $0\nu\beta\beta$ is 2.7×10^{26} yr (90% CL) for an exposure of five years. Compared to the previously published topological cuts [12], our new approach improves the search sensitivity by a factor of 2.4.

Improvement and broader applications the workflow can be expected. Extended Kalman filter (EKF) [23] may take into account of ionization energy loss together with Coulomb scattering processes and estimate the momenta of the particle more accurately. With EKF, one can reconstruct the entire tracks with momentum information along the track, which would be a powerful background suppression tool for background-free searches of ^{136}Xe $0\nu\beta\beta$. The track reconstruction can possibly locate the $0\nu\beta\beta$ vertex, which facilitates the tagging of barium ions in a gaseous TPC [27]. In addition, EKF can be used to determine the energy and angular distributions of the electrons emitted from $2\nu\beta\beta$ and $0\nu\beta\beta$ processes to help understand the decay mechanisms. We envision possible application of the KFB track reconstruction in determining directions of meandering charged particles tracks in general. For example, the direction of Compton or pair-produced electron tracks of γ -ray imaging telescopes [28, 29] can be better reconstructed with our approach. Further development of the reconstruction of meandering track with KFB is warranted.

This work is supported by the grant from the Ministry of Science and Technology of China (No. 2016YFA0400302) and the grants from National Natural Sciences Foundation of China (No. 11775142 and No. 11905127). This work is supported in part by the Chinese Academy of Sciences Center for Excellence in Particle Physics (CCEPP).

† Corresponding author: ke.han@sjtu.edu.cn

- [1] E. Majorana, *Nuovo Cim.* **14**, 171 (1937).
- [2] F. T. Avignone, III, S. R. Elliott, and J. Engel, *Rev. Mod. Phys.* **80**, 481 (2008), [arXiv:0708.1033 \[nucl-ex\]](https://arxiv.org/abs/0708.1033).
- [3] M. J. Dolinski, A. W. P. Poon, and W. Rodejohann, *Ann. Rev. Nucl. Part. Sci.* **69**, 219 (2019), [arXiv:1902.04097 \[nucl-ex\]](https://arxiv.org/abs/1902.04097).
- [4] A. Gando *et al.* (KamLAND-Zen), *Phys. Rev. Lett.* **117**, 082503 (2016), [arXiv:1605.02889 \[hep-ex\]](https://arxiv.org/abs/1605.02889).
- [5] M. Agostini *et al.* (GERDA), *Phys. Rev. Lett.* **125**, 252502 (2020), [arXiv:2009.06079 \[nucl-ex\]](https://arxiv.org/abs/2009.06079).
- [6] D. Q. Adams *et al.* (CUORE), *Phys. Rev. Lett.* **124**, 122501 (2020), [arXiv:1912.10966 \[nucl-ex\]](https://arxiv.org/abs/1912.10966).
- [7] R. Luscher *et al.*, *Phys. Lett. B* **434**, 407 (1998).
- [8] L. Rogers *et al.* (NEXT), *JINST* **13**, P10002 (2018), [arXiv:1804.04116 \[physics.ins-det\]](https://arxiv.org/abs/1804.04116).
- [9] P. Ferrario *et al.* (NEXT), *JHEP* **01**, 104 (2016), [arXiv:1507.05902 \[physics.ins-det\]](https://arxiv.org/abs/1507.05902).
- [10] X. Chen *et al.*, *Sci. China Phys. Mech. Astron.* **60**, 061011 (2017), [arXiv:1610.08883 \[physics.ins-det\]](https://arxiv.org/abs/1610.08883).
- [11] H. Qiao, C. Lu, X. Chen, K. Han, X. Ji, and S. Wang, *Sci. China Phys. Mech. Astron.* **61**, 101007 (2018), [arXiv:1802.03489 \[physics.ins-det\]](https://arxiv.org/abs/1802.03489).
- [12] J. Galan *et al.*, *J. Phys. G* **47**, 045108 (2020), [arXiv:1903.03979 \[physics.ins-det\]](https://arxiv.org/abs/1903.03979).
- [13] P. Matisko and V. Havlena, *Int. J. Adapt. Control Signal Process.* **27**, 957 (2013).
- [14] M. Frosini and D. Bernard, *Nucl. Instrum. Meth. A* **867**, 182 (2017), [arXiv:1706.05863 \[physics.data-an\]](https://arxiv.org/abs/1706.05863).
- [15] S. Agostinelli *et al.* (GEANT4), *Nucl. Instrum. Meth. A* **506**, 250 (2003).
- [16] S. Wang, *JINST* **15**, C03052 (2020), [arXiv:2001.01356 \[physics.ins-det\]](https://arxiv.org/abs/2001.01356).
- [17] C. Xie, K. Ni, K. Han, and S. Wang, (2020), [arXiv:2012.04552 \[nucl-ex\]](https://arxiv.org/abs/2012.04552).
- [18] O. A. Ponkratenko, V. I. Tretyak, and Y. G. Zdesenko, *Phys. Atom. Nucl.* **63**, 1282 (2000), [arXiv:nucl-ex/0104018](https://arxiv.org/abs/nucl-ex/0104018).
- [19] A. Tramacere and C. Vecchio, *Astron. Astrophys.* **549**, A138 (2013), [arXiv:1210.0522 \[astro-ph.IM\]](https://arxiv.org/abs/1210.0522).
- [20] T. Zhang, R. Ramakrishnan, and M. Livny, *SIGMOD Rec.* **25**, 103–114 (1996).
- [21] M. Dorigo and L. M. Gambardella, *IEEE Trans. Evol. Comput.* **1**, 53 (1997).
- [22] R. E. Kalman, *J. Basic Eng.* **82**, 35 (1960).
- [23] R. Frühwirth, *Nucl. Instrum. Methods Phys. Res., A* **262**, 444 (1987).
- [24] C. Patrignani *et al.* (Particle Data Group), *Chin. Phys. C* **40**, 100001 (2016).
- [25] A. Hocker *et al.*, (2007), [arXiv:physics/0703039](https://arxiv.org/abs/physics/0703039).
- [26] F. Alessandria *et al.* (CUORE), (2011), [arXiv:1109.0494 \[nucl-ex\]](https://arxiv.org/abs/1109.0494).
- [27] A. D. McDonald *et al.*, *Phys. Rev. Lett.* **120**, 132504 (2018), [arXiv:1711.04782 \[physics.ins-det\]](https://arxiv.org/abs/1711.04782).
- [28] Y. Mizumura *et al.*, *JINST* **9**, C05045 (2014), [arXiv:1312.0438 \[astro-ph.IM\]](https://arxiv.org/abs/1312.0438).
- [29] P. Gros *et al.*, *Astropart. Phys.* **97**, 10 (2018), [arXiv:1706.06483 \[astro-ph.IM\]](https://arxiv.org/abs/1706.06483).

* Corresponding author: shaobo.wang@sjtu.edu.cn